Flexible, self-powered, magnetism/pressure dual-mode sensor based on magnetorheological plastomer

Jiaqi Xu[a], Lei Pei[a], Jun Li[b], Haoming Pang[a], Zhiyuan Li[b], Binshang Li[b], Shouhu Xuan[a],[**], Xinglong Gong[a],[*]

[a] CAS Key Laboratory of Mechanical Behavior and Design of Materials, Department of Modern Mechanics, CAS Center for Excellence in Complex System Mechanics, University of Science and Technology of China, Hefei, 230027, China
[b] Anhui Weiwei Rubber Parts Group Co.Ltd., Tongcheng, 231400, China

ABSTRACT

A flexible self-powered magnetism/pressure dual-mode sensor, which consists of magnetorheological plastomer (MRP), was developed in this work. The working mechanism of the self-powered sensor was based on the displacement reaction of Fe and $CuSO_4$. Different from traditional flexible pressure sensors, it was not only sensitive to a slight pressure (1.3 kPa), but also responsive to a small magnetic field (12 mT). Under an external magnetic field, the micro-scale carbonyl iron (CI) particles in the MRP electrode aggregated into the chain-like and the cluster-like structures, which enhanced the electrochemical activity of ions in the electrolyte of the electrode materials and formed the conductive network. The voltage increased with the magnetic field strength and the sensitivity was 4.2% at a 252 mT magnetic field. To further explore the mechanism of sensor, the microstructure evolution of CI particles inside the electrode materials under different magnetic fields was simulated by particle-level dynamics method. Finally, a smart writing board based on a self-powered magnetism/pressure dual-mode sensor array was developed and it was sensitive to different magnetic fields without an external power supply, which demonstrated a broad potential for mobile electronic device in the non-contact state.

1. Introduction

The pressure sensor is the device which generates electrical signal in response to mechanical stimulate. Capacitance [1,2], piezoresistive [3,4], and piezoelectric [5,6] are the most common methods for signal transmission. In particularly, flexible pressure sensors have become a hot issue in personal health monitoring [7,8], human motion detection [9,10], electronic skin [11,12], and intelligent robot [13,14], due to their softness, slight weight, and facile interaction with the human body. Recently, many high-sensitive, fast-responding, wearable flexible pressure sensors have been developed. A flexible piezoresistive sensor composed of an elastomer film and CNT composites can be highly sensitive to a small pressure of 0.2 Pa [15]. The flexible pressure sensor, prepared by the reduced graphene oxide and polyaniline wrapped sponge, can respond to external stimuli in 96 ms [16]. Typically, these flexible pressure sensors were wearable to monitor the human joint movement in fast time and they could also provide signal feedback for small pressures.

To implement the mobility of flexible pressure sensors, self-powered sensing systems are highly desirable because they do not require an external power source. Self-powered sensing devices such as tribo-electric sensor [17,18], piezoelectric sensor [19,20], and super-capacitor [21,22] are growing rapidly nowadays. Triboelectric materials and piezoelectric materials such as zinc oxide [23,24], PVDF [20,25], etc. are able to induce electric charges on the surface when a mechanical stimulus is applied, thus they are widely used in flexible pressure sensors due to their softness and sensitivity. Recently, many self-powered sensing devices have also been constructed by super-capacitor. Under the external force, the plate spacing of the capacitor changes due to mechanical deformation, resulting in a capacitance variation. Due to the advantage of small size, light weight and high efficiency, the supercapacitor has attracted attentions in flexible pressure sensors. In addition, it is well known that the battery is self-powered. Most of the previous reports were focused on exploring various types of stretchable and flexible batteries, such as silver-zinc batteries [26], zinc-manganese batteries [27], and lithium batteries [28].

However, these stretchable and flexible batteries have been separably applied as energy storage devices for wearable electronic devices. The sensing characteristics of the flexible battery itself according to the external stimuli has rarely been reported.

With the rapid development of electronic technology and artificial intelligence, the demand for multifunctional sensors is more urgent. To mimic the tactile sensations of human skin and limbs, flexible sensors are eager to detect multiple stimuli such as pressure, temperature, strain, and humidity [29]. The dual-mode sensor integrating responses of different stimuli into a single device is under increasing requirement in the field of electronic skin and smart electronics [30]. Park J.U. reported a novel mobile smart device and the as-prepared flexible dual-mode sensor array could simultaneously detect both tactile pressure and finger skin temperature [31]. Magnetic field sensing is a non-polluting, non-contact, fast response, adjustable sensing method with wide applications in non-destructive testing, remote control, real-time monitoring [32–35]. Recently, Fu S.Y. developed a magnetic-strain dual mode sensor by adding magnetic particles into a conductive polymer. Interestingly, the dual mode sensor exhibited the capacity of identifying the contact and contactless state [36]. In addition, some biomimetic structures, such as cilia, with magnetic particles and graphene, also exhibited the high-sensitive dual-mode response to pressure and magnetic field. Obviously, this biomimetic dual mode sensor showed a great potential in healthcare and smart surgical tools [37]. However, owing to the solidified polymer matrix constraint, the magnetic particles were fixed in the sensors and the particles' movability were very weak, which often led to a negative effect on the efficiency of the magnetism sensor [38].

The magnetorheological plastomers (MRP) is a kind of magneto-controllable soft material made up of the low cross-linking density polyurethane (PU) and magnetic CI particles. Under the magnetic fields, the magnetic CI particles can be easily moved to form chain-like structures, which greatly contributes to the change of the mechanical and electrical properties [39,40]. MRP is soft, highly sensitive, magneto-sensitive, and adjustable, thus it possesses high potential in the field of magnetic sensing sensors [41,42]. Previously, Pang H.M. developed a smart magneto-controllable switch by doping conductive materials into the MRP. The results indicated that the electric resistance of the conductive MRP was very sensitive to the external magnetic field [43]. Therefore, due to the high flexibility, force sensitivity, and magnetic field dependent conductivity, the MRP is expected for high performance dual mode sensor with self-powered characteristic.

In this work, a flexible self-powered magnetism/pressure dual-mode sensor based on MRP was developed. The dual-mode sensor, which exhibited the advantages of high flexibility, magnetic sensitivity, and self-powered characteristic, was fabricated by the electrode (composed of MRP, graphite, NaCl and $CuSO_4$), separator, and substrate (PET film). Fast response to pressure and magnetic fields were essential features of the sensor. Therefore, it could monitor a weak dynamic pressure and human joint motion. Furthermore, the microstructure evolution of CI particles inside the electrode was simulated by particle-level dynamics method, and the working mechanism of the sensor under the pressure and magnetic field was discussed. Specifically, a smart magnetic sensing writing board manufactured by the flexible dual-mode magnetism/pressure sensor array showed an application in the field of contactless electronics.

2. Experimental

2.1. Materials

The raw materials for the synthesis of polyurethanes (the matrix of MRP) included polypropylene glycol (PPG-1000, Sinopec Group Co. Ltd., China), toluene diisocyanate (TDI, 2,4-TDI at B80%, 2,6-TDI at B20%, Tokyo Chemical Industry Co. Ltd., Japan), and Diethylene glycol (DEG, Sinopharm Chemical Reagent Co. Ltd., Shanghai, China). Copper

powders, $CuSO_4$ were used for the cathode electrode, and CI particles (type CN, BASF aktiengesellschaft, Germany), NaCl were used for the anode electrode. Graphite (Tanfeng Graphene Technology Co. Ltd. Suzhou, China) was added to the electrode to improve conductivity. Sodium dodecylbenzene sulfonate and acetone were used as active agents and dispersing solvents, respectively. In addition, the separator (a polypropylene film), PDMS film and PET film in sensor were purchased from Celgard Co. Ltd. in America and BALD Advanced Materials Co. Ltd. in Hangzhou, China and Yuanhao Office Co. Ltd. in Shanghai, China.

2.2. Preparation of anode and cathode materials

The matrix of MRP was a homemade PU synthesized by mixing TDI and PPG in a molar ratio of 3:1 at 80 °C for 2 h and then DEG was added at 60 °C within 30 min. The synthesized PU was sufficiently dissolved in acetone to a clear solution. NaCl solution (2 mol L^{-1}), 50 wt% CI particles and an appropriate amount of graphite were added into the PU solution with ultrasonic treatment for 24 h to form slurry. At last, the mixture was dried at 50 °C to remove excess water and acetone. The anode material (MRP electrode) like a plasticine was prepared. The cathode material ($CuSO_4$/PU electrode) can be prepared by mixing 1 mol L^{-1} $CuSO_4$ solution, copper powder, graphite, and PU solution according to the same method.

2.3. Fabrication of the self-powered magnetism/pressure dual-mode sensor

A copper foil and a copper wire were adhered to the PET film to form a conductive electrode. In order to encapsulate the MRP electrode materials and $CuSO_4$/PU electrode materials, a PDMS film frame of 2 cm × 2 cm was closely attached to the copper foil. The MRP electrode materials and $CuSO_4$/PU electrode materials were filled in the grooves and combined with the separator to form a flexible self-powered dual-mode magnetism/pressure sensor. The separator can prevent the short circuit caused by direct contact between the MRP electrode materials and $CuSO_4$/PU electrode materials. The ions in the electrolyte of the electrode materials were free to pass through the separator.

2.4. Characterizations

The morphologies of MRP electrode and $CuSO_4$/PU electrode materials were imaged by a scanning electron microscope (SEM, Gemini 500, Carl Zeiss Jena, Germany). All optical images were taken by a digital camera (D1700, Nikon). The rheological properties of MRP and electrode materials were measured by a commercial rheometer (Physica MCR301, Anton Paar Co., Austria) equipped with a magneto-controllable accessory MRD180 in shear oscillation mode. An electronic universal testing machine (RGM 6005T, REGER) was used to measure the pressure sensing performance of the sensor at different pressures and compressive rates. The voltage signal was collected by a digital multimeter (Keithley 2000). The bending testes of the sensor at 5 Hz frequency were implemented by the Dynamic Mechanical Analyzer (TA Electro Force 3200 series, America). The magnetic flux density was changed from 0 to 206 mT in magnetic sensing tests by adjusting an electromagnetic coil current from 0 to 4 A, which was regulated by a DC power supply (ITECH IT6724).

3. Results and discussion

The flexible dual-mode magnetism/pressure sensor was composed of PET films, copper foil electrodes, MRP electrode, $CuSO_4$/PU electrode and a separator (Fig. 1a). Two copper wires were respectively extended from two copper foil electrodes for transmitting electrons (Fig. 1b). Multi-layer sensor was only 1.2 mm thick, which was soft and suitable for human body wear (Fig. 1f and g). Fig. 1c–e showed the microscopic morphology of electrode materials with and without a
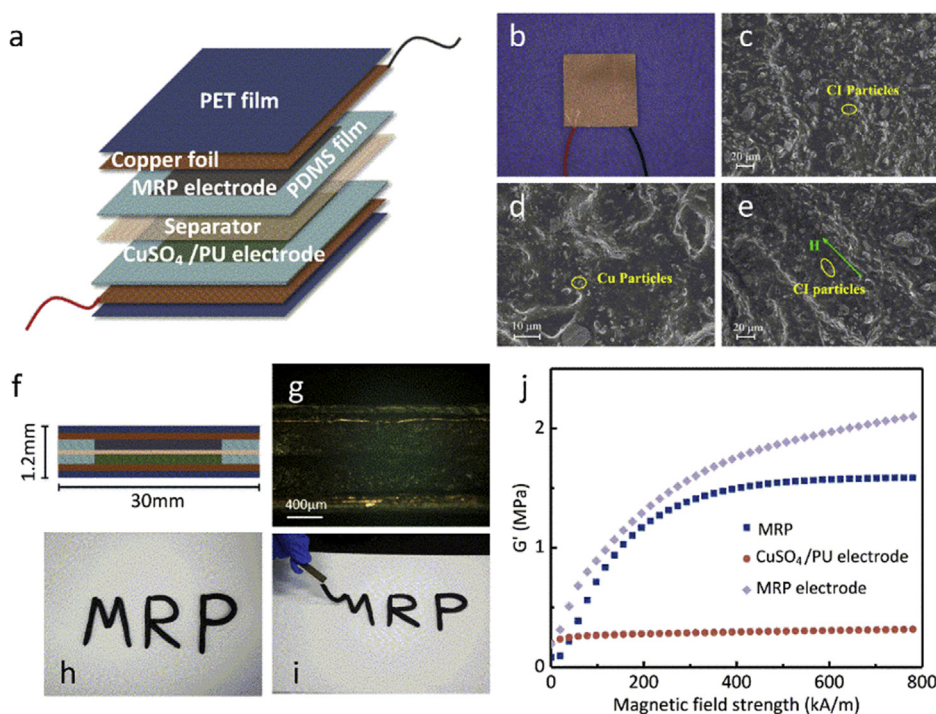
Fig. 1. (a) Schematic illustration and (b) digital photograph of the dual-mode sensor. The SEM images of (c) MRP electrode without and (e) with a magnetic field, (d) $CuSO_4$/PU electrode. (f) Schematic illustration and (g) microscopic morphology of the dual-mode sensor cross section. (h) Digital photographs of MRP electrode with plasticity and (i) magnetism. (j) The storage modulus of MRP, $CuSO_4$/PU electrode, MRP electrode under different magnetic field strength.

magnetic field. The CI and the copper powder particles were uniformly distributed in the MRP electrode and $CuSO_4$/PU electrode, respectively. The SEM images of CI particles, copper powder, and graphite were showed in Fig. S1. The average sizes of them were 7 μm, 4 μm and 800 nm, respectively. When a magnetic field was applied, the CI particles were assembled to chains structure along the direction of the magnetic field (Fig. 1e).

Due to the famous magnetorheological (MR) effect, the storage modulus of the MRP increased with the magnetic field (Fig. 1j). Here, the MRP electrode showed the MR behavior because of the magnetic assembling process. As a contrary, the $CuSO_4$/PU electrode showed a stable rheological property under a magnetic field. Graphite in the both electrodes was uniformly attached to the PU molecular network, which not only enhanced the electron transportation inside the electrodes but also improved the mechanical properties. The initial storage moduli of the MRP electrodes was higher than MRP since the particle (graphite)-strengthen phenomenon [43–45]. Under applying an external magnetic field, CI particles in MRP electrode formed chain-like structures along the magnetic field. As the magnetic field strength increased, the CI particle chains were compact, and the storage modulus of MRP electrode increased. As shown in Fig. 1h and i, the plastic MRP electrode showed a typical magneto-sensitive property. More importantly, the both electrodes were composed of low cross-linking density PU polymer, the plastic characteristics enabled the electrodes to exhibit good self-healing property (Fig. S2).

The piezoelectric performance of the sensor was tested by the electronic universal testing machine (RGM 6005T REGER, Fig. 2a). The voltage of the sensor with a pressure was exhibited in Fig. S3. Fig. 2b and c showed the change in voltage of the sensor with different pressures and compression rates. Voltage variation at smaller pressure (1.3–5.1 kPa) was showed in Fig. S4. Significant and stable voltage variation indicated the high responsibility and excellent reliability of the sensor. As shown in Fig. 2d, with the pressure increased from 1.3 to 38.2 kPa, the increase of voltage exhibited two characteristic trends. The ratio of the voltage variation to pressure in the low-pressure regime (1.3–6.4 kPa, β = 1.33) was higher than that in the large-pressure regime (6.4–38.2 kPa, β = 0.32). The voltage variation and pressure satisfy the following formula:

$$\Delta U = \begin{cases} 1.33P + 0.50, & 0 < P \ll 6.4 \ kPa \\ 0.32P + 7.08, & 6.4 \ kPa < P \ll 38.2 \ kPa \end{cases} \tag{1}$$

Where ΔU represented the increment of voltage, and P represented the pressure. Obviously, the changes in voltage, pressure and displacement occurred synchronously (Fig. 2e).

Fig. 2f explained the working mechanism of the sensor under a pressure. The voltage variation of the sensor was based on an electrochemical reaction between the anode electrode materials and the cathode electrode materials. The blue sphere and pink ellipsoid represented CI particles and copper powder particles, respectively. The yellow, orange, light green and dark green dots were Na^+, Cl^-, Cu^{2+} and SO_4^-. The displacement reaction of Fe (CI particle) and $CuSO_4$ occurred in the electrode. The electrochemical activity of ions in the electrolyte of the electrode materials was critical to the voltage variation of the sensor. The microstructures in electrode materials of the sensor were changed by CI particles and copper powder particles, which enhanced the electrochemical activity of ions in the electrolyte of the electrode materials and caused an increase in voltage. This sensor can provide voltage signal feedback for a pressure of 1.3 kPa, which has a good prospect in the application field.

Owing to the sensitivity of the sensor, it can detect the slight and rapid human action and object motion. Fig. 3a and b showed the signals of the sensor under continuous light pat and click. Clearly, the sensor can respond to the external stimuli, thus the moving behavior can be captured continuously and accurately. More importantly, the disturbances caused by the slight pressure on the electrodes can be quickly recovered after decompression. Therefore, the sensor is of high potential in stress detection. Furthermore, by embedding the sensor device in the "road", it was possible to detect the travel of the "car" with a small weight of only 17 g (Fig. 3c). Embedding multiple sensor into the "road" generated different voltage signals separately when the "frog" passed (Fig. 3d). This can obtain the speed of "frog" by measuring the time between the different signals and the length of the "road".

To further study the performance of the sensor, the bending tests were implemented by ElectroForce 3200. Both ends of the sensor were clamped, of which one end was fixed and the other end was moved downward at a frequency of 5 Hz. A digital multimeter was used for data acquisition. Multiple cyclic bending tests were conducted at the
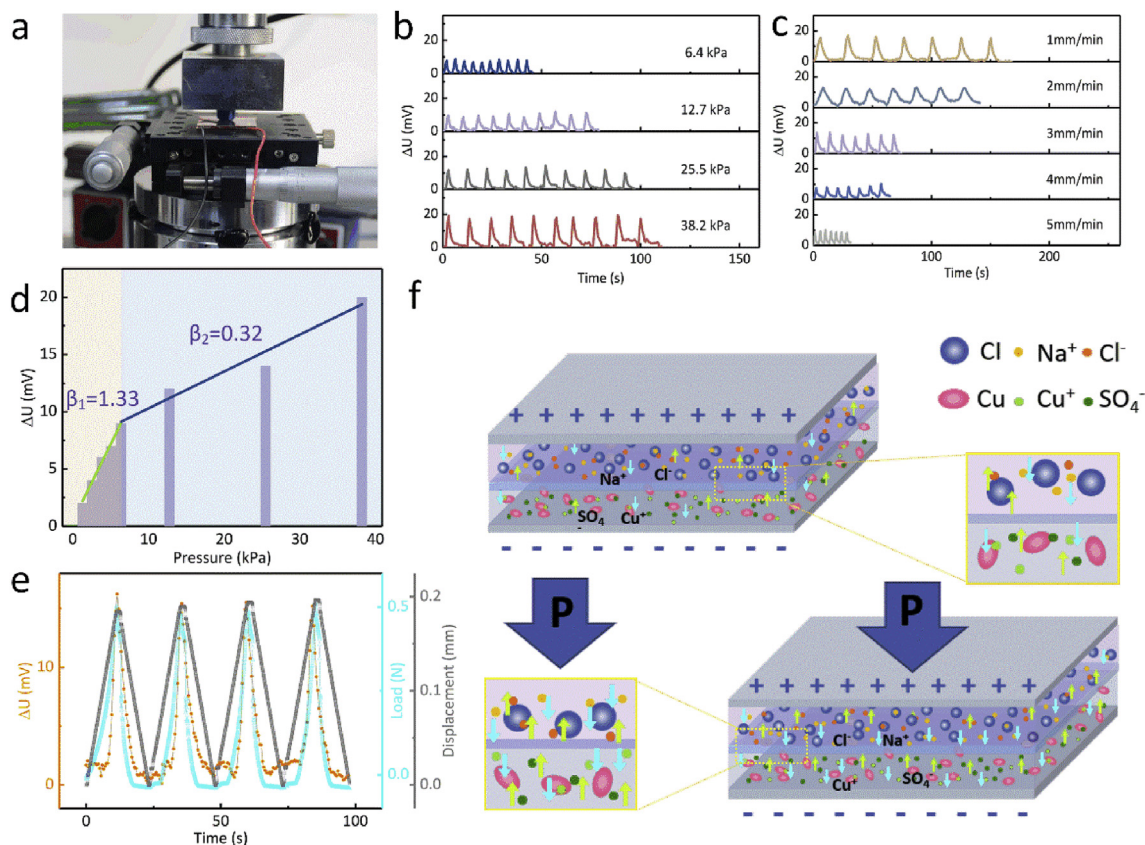
Fig. 2. The pressure sensing of dual-mode sensor under the compression stimuli. (a) The photograph of the device for compression testing. (b) Voltage variations of the sensor at different pressures (compressive rate was 5 mm/s) and (c) compressive rates (pressure was 6.4 kPa). (d) Voltage variations at the pressure of 1.3–38.2 kPa. (e) Consistency of voltage, pressure, and displacement over time. (f) Schematic diagram of the microscopic change of the dual-mode sensor under the pressure. The small blue and green arrows indicated the ion transfer process. (For interpretation of the references to color in this figure legend, the reader is referred to the Web version of this article.)
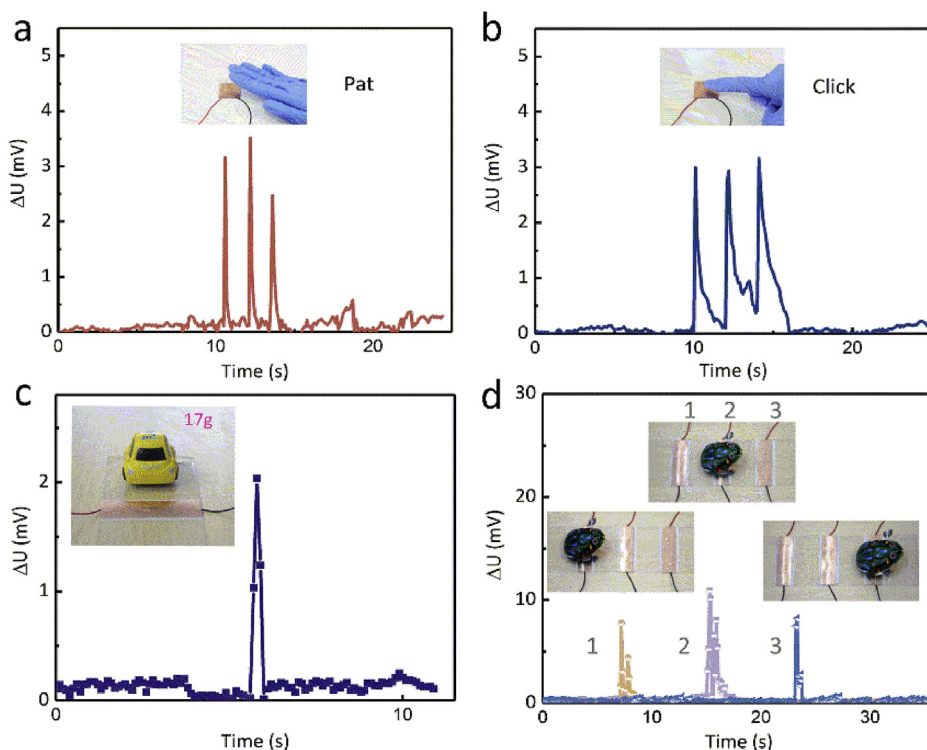

Fig. 3. Dynamic behavior monitoring of human bodies and objects: (a) pat, (b) click, (c) "car" driving, (d) "frog" jumping continuously.
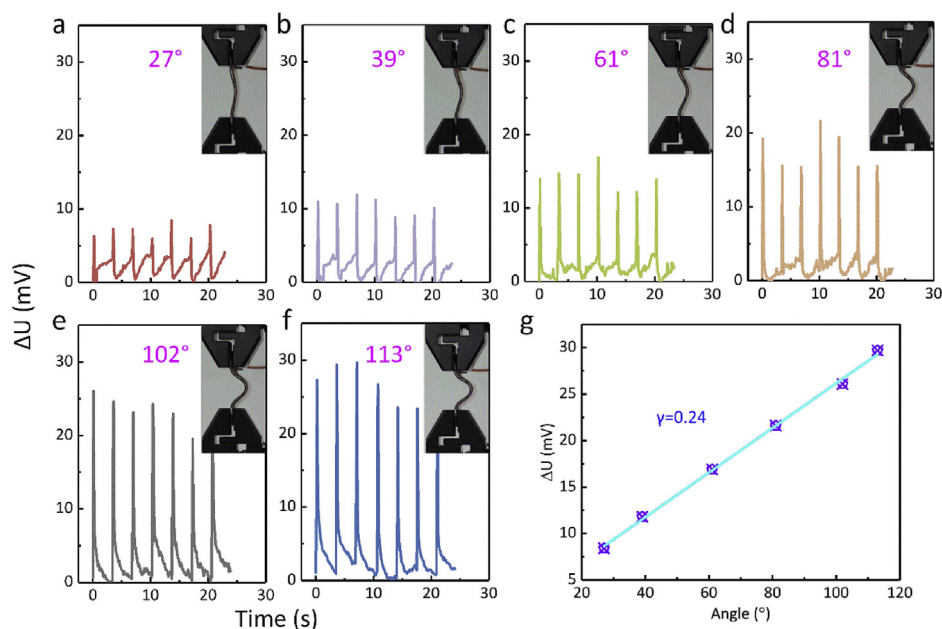
Fig. 4. Digital Photographs and voltage variation of the dual-mode sensor at the bending angles of (a) 27°, (b) 39°, (c) 61°, (d) 81°, (e) 102°, (f) 113°, respectively. (g) Voltage variation at different bending angles.

bending angles of 27°, 39°, 61°, 81°, 102°, 113° (Fig. 4a–f). Clearly, the voltage increased from about 7 to 30 mV along with the bending angles increased from 27 to 113°. The sensor signal was stable and repeatable in several bending cycles. Fig. 4g presented the voltage variation is linear with the angle. The slope (γ) was calculated to be 0.24. The increment of voltage was:

$$\Delta U = 0.24\,\theta + 2.15 \tag{2}$$

Where ΔU represented the increment of voltage, and θ represented the angle. This sensor was well adapted to different bending angles and it can be also used as a reliable bending sensor.

Furthermore, based on the soft and bendable sensitive behavior, the sensor can serve as the wearable device to monitor joint actions. As shown in Fig. 5, the sensor was fixed on the finger and the voltage varied with the movement of the joint. As the size of beakers gripped by fingers increased, the voltage variation of sensor on the fingers rose respectively. As shown in Fig. 5f–j, once the fingers grabbed the beaker, the voltage began to increase and then kept stable. With a smaller beaker, large bending angle existed in the finger, thus a larger voltage signal was obtained. There was a good consistency between force

loading and sensor response. Therefore, the sensor can be applied to accurately monitor the human joint motions due to its excellent sensitivity and flexibility.

Interestingly, the sensor also exhibited a unique sensitivity to the magnetic field due to the CI particles in MRP electrode. The device of magnetic sensing test was shown in Fig. 6a, which was composed of an electromagnet, a DC power supply, a digital multimeter, a program control system and a data storage device. The magnetic field strength was changed by adjusting the current of the electromagnet coil, which was regulated by the DC power supply. Fig. 6b showed the continuous and stable voltage response of the sensor with the magnetic field strength ranged from 54 to 206 mT. The voltage changed with the magnetic field was instantaneous without hysteresis (Fig. 6c). As shown Fig. 6d, the increment of voltage varied from 0.5 to 28 mV with the magnetic field strength from 12 to 252 mT. When the magnetic field was applied, the CI particles uniformly distributed on the MRP electrode easily assembled to chain-like structures due to the low crosslinking degree of the matrix. Together with the graphite, the chain-like CI particles structures along the direction of the magnetic field formed
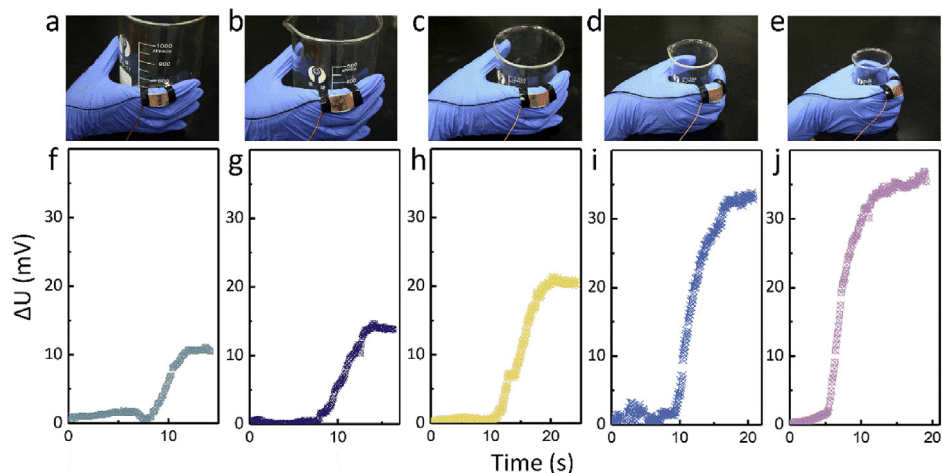

Fig. 5. Real-time monitoring of human joint activity. (a–e) Fingers wearing dual-mode sensors grasp different range beakers, (f–j) corresponding voltage variation.
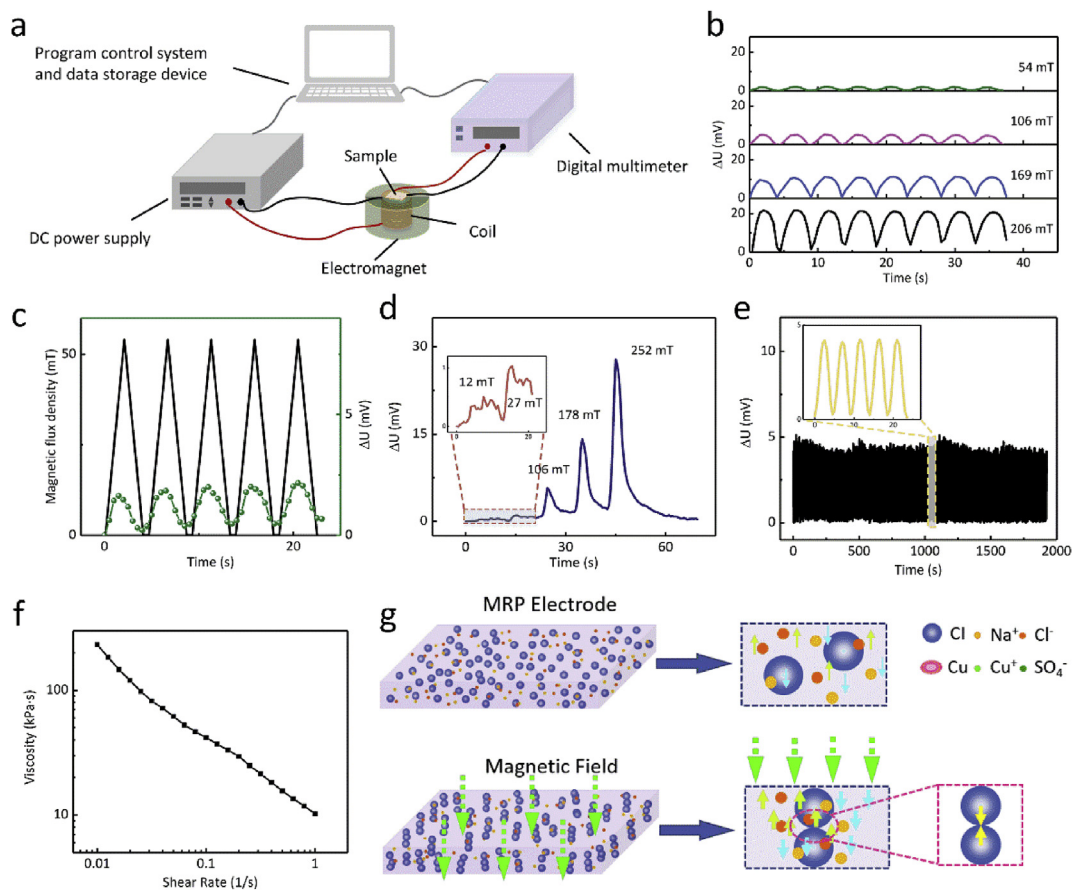
Fig. 6. The voltage response of dual-mode sensor under the magnetic field. (a) Schematic diagram of the magnetic sensing testing system. (b) Voltage variation of dual-mode sensor under the different magnetic flux density. (c) Real-time response to magnetic flux density and voltage variation. (d) Voltage changes under increasing magnetic field. (e) Voltage response under magnetic field on-off cycle. (f) The viscosity of the matrix. (g) Schematic diagram of the microscopic change of the dual-mode sensor under a magnetic field.

the conductive network, which facilitated the transmission of electrons in electrochemical reactions. Furthermore, because of the magneto-in-duce stress between the CI particles, the connection between the electrode material and the electrode plate was closer and the performance of electrochemically active molecules were increased to a great extent (Fig. 6g) [46]. Therefore, the voltage variation of the sensor was sensitive to the magnetic field.

Because the electromagnet was very easy to be heat up severely under a large current for a long time, the magnetic sensing cyclic test with a 83 mT magnetic field was performed (as a representative of the small magnetic flux density interval of Fig. 7a). The increment of the voltage kept almost a constant under a 500-cycles magnetic field application, implying the reliability and stability of the sensor (Fig. 6e). More discussion of the magnetic properties of the sensor was shown in Figs. S5 and S6. When a magnetic field was applied, the CI particles uniformly distributed in the electrode gradually moved along the direction of the magnetic field. Once the magnetic field was turned off, the CI particles remained in position due to the constraints of the matrix (Fig. 6f). At this time, the voltage was increased compared the initial value due to the change in the position of the CI particles. As the magnetic field was turned on again, the CI particles continued to move in the direction of the magnetic field. After several cycles, the CI particles formed stable chain-like structures and the voltage value increased or decreased to a stable value when magnetic field was on or off.

In order to explore the magnetic sensing mechanism of the sensor, further exploration was conducted. Fig. 7a showed the relationship between the increment of voltage and magnetic flux density. Here the α

was defined as the ratio. With 106 mT as the boundary, two sensitive regions of 0.05 and 0.16 were presented. The increment of voltage can be calculated as:

$$\Delta U = \begin{cases} 0.05B - 0.33, & 0 < B \ll 106 \ mT \\ 0.16B - 13.48, & 106 < B \ll 252 \ mT \end{cases} \tag{3}$$

Where ΔU represented the increment of voltage, and B represented the magnetic flux density. The magnetization curves of CI particles and MRP electrode materials were exhibited in Fig. 7b. The saturation magnetization of the MRP electrode with 50 wt% CI particle content was almost half of the CI particle, which reflected that the magnetic properties of the CI particle inside the MRP electrode were substantially unchanged.

The reorganization of CI particles under different magnetic fields was simulated by the particle-level dynamic method. When a uniform magnetic field $\boldsymbol{H}$ was applied, the magnetic moment $\boldsymbol{m}_i$ of a CI particle i was expressed as:

$$\boldsymbol{m}_i = MV_i \frac{\boldsymbol{H}}{H} = M_S(1 - e^{-\chi H})V_i \frac{\boldsymbol{H}}{H} \tag{4}$$

Here, M was the magnetization of the CI particle. $V_i = \pi d_i^3/6$ was the volume of the particle i, and d_i was the diameter of the particle i. $\chi = 4.91 \times 10^{-6}$ m/A was a constant. A magnetic field $\boldsymbol{H}_i$ generated by magnetized particle i was described as:

$$\boldsymbol{H}_i = -\frac{1}{4\pi r^3}[\boldsymbol{m}_i - 3(\boldsymbol{m}_i \cdot \hat{\boldsymbol{r}})\hat{\boldsymbol{r}}] \tag{5}$$

Where r represented the position vector from the particle i to a position point. $r = |\boldsymbol{r}|$ and $\hat{\boldsymbol{r}} = \boldsymbol{r}/r$. Once another particle was placed in the
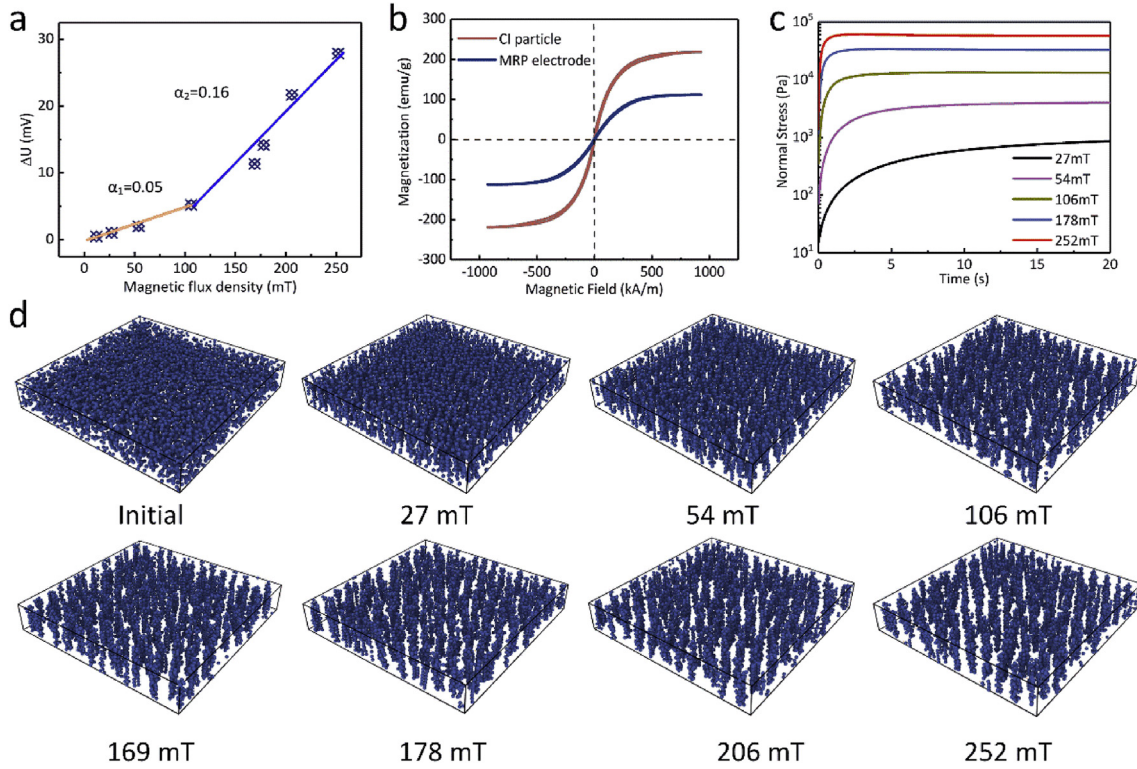
Fig. 7. (a) Voltage variation under different magnetic flux density. (b) Magnetization curves of CI particles and MRP electrode. (c) Normal stress of MRPelectrode under different magnetic fields. (d) Microstructural evolution of CI particles inside MRP electrode under the magnetic fields of 27 mT, 54 mT, 106 mT, 169 mT, 178 mT, 206 mT, 252 mT.

magnetic field H_i, it was magnetized by the particle i. According to the superposition method, the magnetic moment of a particle was:

$$\boldsymbol{m}_i = M_S\left(1 - e^{-\chi H_l}\right)V_i\frac{\boldsymbol{H}_l}{H_l}, \quad \boldsymbol{H}_l = \boldsymbol{H} + \sum_{j \neq i}\boldsymbol{H}_j$$

(6)

The magnetic dipole force of the particle i generated by the particle j was:

$$\boldsymbol{F}_{ij}^m = \frac{3\mu_0}{4\pi r_{ij}^4}c_m[(-\boldsymbol{m}_i\cdot\boldsymbol{m}_j + 5\boldsymbol{m}_i\cdot\boldsymbol{t}\boldsymbol{m}_j\cdot\boldsymbol{t})\boldsymbol{t} - (\boldsymbol{m}_i\cdot\boldsymbol{t})\boldsymbol{m}_j - (\boldsymbol{m}_j\cdot\boldsymbol{t})\boldsymbol{m}_i]$$

(7)

Here, r_{ij} was the distance between two particles. The magnetic permeability of the matrix was approximately equal to $\mu_0 = 4\pi \times 10^{-7}$ H/m. $\boldsymbol{t}$ was the unit vector pointing from particle i to particle j. c_m was the correction factor of the point dipole model [47,48].

$$c_m = \begin{cases} 1 + \left(3 - \frac{2r_{ij}}{d_{ij}}\right)^2\left[\frac{0.6017}{1 + e^{\frac{(|\theta| - 34.55)}{12.52}}} - 0.2279\right] & r \leq 1.5d_{ij} \\ 1 & r > 1.5d_{ij} \end{cases}$$

(8)

Here, θ was the angle between $\boldsymbol{t}$ and $\boldsymbol{H}$. $d_{ij} = (d_i + d_j)/2$. The van der Waals force between the two CI particles was [49]:

$$\boldsymbol{F}_{ij}^{vdW} = \frac{8A}{3}L_{ij}d_id_j\left[\frac{1}{4L_{ij}^2 - (d_i + d_j)^2} - \frac{1}{4L_{ij}^2 - (d_i - d_j)^2}\right]^2\boldsymbol{t}$$

(9)

Here, A$= 5 \times 10^{-19}$ was the Hamaker constant of CI particles. $L_{ij} = max\left[r_{ij}, \quad d_{ij} + h_{min}\right]$, $h_{min} = 0.001d_{ij}$ [50]. To characterize the squeezing and collision between particles and prevent the overlapping of particles, the repulsive force was introduced as follows:

$$\boldsymbol{F}_{ij}^r = -\left(\xi\frac{3\mu_0 m_{si}m_{sj}}{4\pi d_{ij}^4} + \boldsymbol{F}_{ij}^{vdW}\right)10^{-10\left(\frac{r_{ij}}{d_{ij}} - 1\right)}\boldsymbol{t}$$

(10)

m_{si} and m_{sj} were the saturation magnetization of the target particles. To offset the magnetic dipole force and van der Waals force when the two

particles were connected end to end along the magnetic field, $\xi = 2$.

The matrix was approximated as a Bingham plastic fluid. When Re = 0, the CI particles began to move in the Bingham fluid, following the condition as [51]:

$$\sum F \geq 3.5\tau_y\pi d_i^2$$

(11)

Where τ_y was the yield stress of the matrix and $\sum F$ was the resultant force. Neglecting Brownian motion, particle-matrix interactions included drag force and buoyancy. When the driving force was greater than this value, the drag coefficient was [52]:

$$\frac{F_i^d}{3\pi\eta d_i v} = 1 + 2.93(\text{Bn})^{0.83}$$

(12)

Where η was the viscosity of the matrix, and F_i^d was the drag force. v was the velocity of the particle relative to the matrix. $Bn = \frac{\tau_y d_i}{\eta v}$ was the Bingham number. The gravity and buoyancy of the particles was:

$$\boldsymbol{F}_i^{gb} = \frac{\pi d_i^3}{6}(\rho - \rho_0)\boldsymbol{g}$$

(13)

Where ρ and ρ_0 was the density of the particles and matrix, respectively.

Due to the CI particle was the soft magnetic material, the magnetic torque on the particles was so small that the particle rotation could be ignored. The inertia and acceleration of the particles were also not taken into account. In view of the aforementioned forces, the kinematic equation was established as follows:

$$\sum_{j \neq i}(\boldsymbol{F}_{ij}^m + \boldsymbol{F}_{ij}^{vdW} + \boldsymbol{F}_{ij}^r) + \boldsymbol{F}_i^d + \boldsymbol{F}_i^{gb} = \boldsymbol{0}$$

(14)

The magnetic-induced stress tensor $\boldsymbol{\sigma}$ and the magnetic potential energy U_m were expressed as:

$$\boldsymbol{\sigma} = \frac{1}{V}\sum_i\sum_{j>i}\boldsymbol{r}_{ij}\boldsymbol{F}_{ij}$$

(15)

$$U_m = \mu_0 \sum_i \left[-\boldsymbol{m}_i \cdot \boldsymbol{H} + \sum_{j>i} \frac{1}{4\pi r_{ij}^3} (\boldsymbol{m}_i \cdot \boldsymbol{m}_j - 3\boldsymbol{m}_i \cdot \boldsymbol{t} \boldsymbol{m}_j \cdot \boldsymbol{t}) \right] \tag{16}$$

Here V was the volume of the simulation box. $\boldsymbol{r}_{ij}$ and $\boldsymbol{F}_{ij}$ represented the position vector and the interaction force between a pair of particles. The stress tensor and magnetic potential energy depended on the particle position, interaction and distribution in the matrix, which reflected the evolution of the microstructure.

As shown in Fig. 7c, the magneto-induced stress between the CI particles increased with the magnetic flux density. When the magnetic flux density was larger than 100 mT, the stress rapidly increased to the maximum value and kept as a constant, which meant that the CI particles can be magnetized instantaneously. Particularly, the variation of the chain-like structures of the CI particles assembled under different magnetic flux densities were simulated (Fig. 7d). With increasing of the magnetic flux density, CI particles gradually formed clear chain-like structures. Moreover, under a larger magnetic flux density (106 mT, 169 mT, 178 mT, 206 mT, 252 mT), the cluster-like structures became more strengthened. Since the CI particles moved rapidly to form more pronounced chain or cluster-like structures under a larger magnetic field, the ions in the electrolyte of the electrode materials were more electrochemically active, and the voltage variation was larger.

This magnetic field dependent sensor was favorable for smart displaying devices. Here, the dual-mode sensor was extended to an array configuration of several pixels to describe the comprehensive magnetic sensing information. Schematic illustration of the fabrication processes was showed in Fig. S7. As shown in Fig. 8a, a smart writing board consisted of a 5 × 5 element magnetic sensor matrix (Fig. 8c) and a magnetic pen (Fig. 8b) was constructed. When a magnetic pen that could generate a local magnetic field moved to a certain unit of sensor element, the voltage increased, while the voltage of others untouched remained constant. Therefore, when the word was written with a magnetic pen on the writing board, the signal of the voltage variation was collected. Fig. 8d presented the handwritten words of "U" "S" written under a 120 mT magnetic pen and "T" "C" written under an 84 mT magnetic pen. Clearly, "U" and "S" showed dark red color and the "T" and "C" were pink, respectively. As magnetic field was lager, the voltage variation was lager. To this end, the present dual-mode sensor was expected to have broad application in electronic devices.

4. Conclusions

A flexible self-powered magnetism/pressure dual-mode sensor has been reported by using MRP, graphite, NaCl and CuSO$_4$ as electrode materials. This multifunctional sensor can sense to both pressure and magnetic fields without an external power supply. The sensor also exhibited the high sensitivity of a slight pressure (1.3 kPa) and a small angle bending (27°). It can detect the human joints motion and the objects movement due to excellent stability and response. The CI particles inside the electrode material aggregated into chain-like and cluster-like structures under a magnetic field. The voltage variation increased gradually as the magnetic field strength increased. It provided a response to magnetic field and reached a sensitivity of 4.2%/252 mT. The arrangement of CI particles in the electrode material under magnetic field was analyzed by particle-level dynamics method. As the magnetic field increased, the particle chains became more compact to form cluster structures, which explained the magnetic response mechanism of the sensor very well. Finally, a magnetic sensing smart writing board assembled by the sensor array was developed. This flexible self-powered dual-mode magnetism/pressure sensor exhibited a great potential in intelligent electronic device such as personal health monitoring, soft robots, and mobile electronics.

Appendix A. Supplementary data

Supplementary data to this article can be found online at https://doi.org/10.1016/j.compscitech.2019.107820.
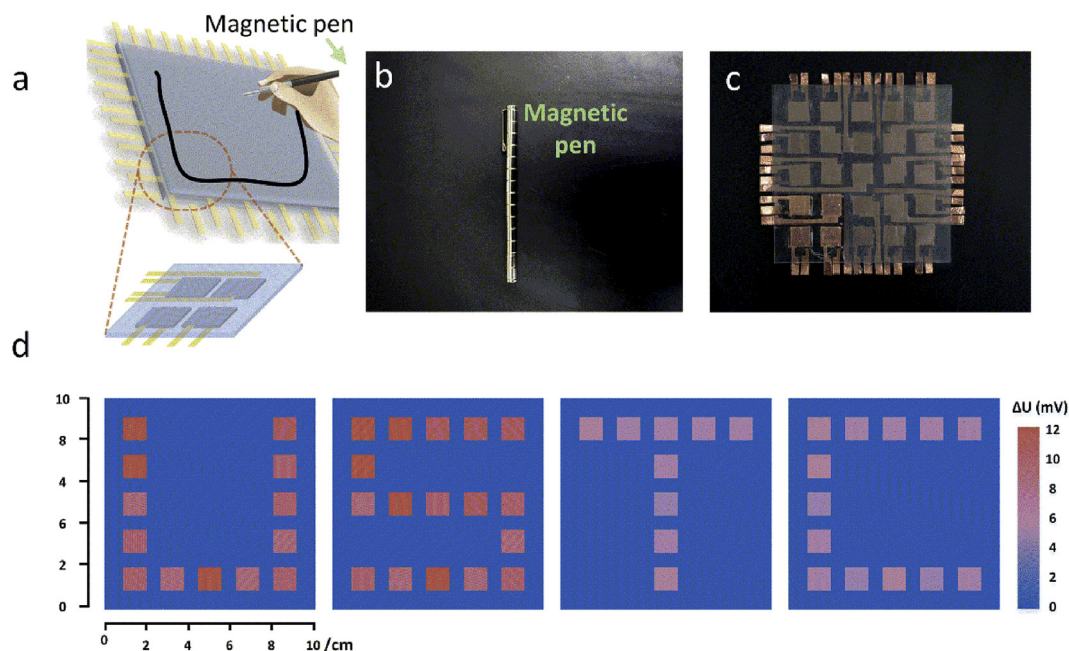

Fig. 8. (a) Schematic illustration of a smart writing board composed of a dual-mode sensor array. (b) Photographs of the magnetic pen and (c) dual-mode sensor array. (d) Voltage change profile. Write the words "U" and "S" under 120 mT magnetic field and "T" and "C" under 84 mT magnetic field.

References

[1] S. Yao, Y. Zhu, Wearable multifunctional sensors using printed stretchable conductors made of silver nanowires, Nanoscale 6 (4) (2014) 2345–2352.

[2] B. You, C.J. Han, Y. Kim, B.-K. Ju, J.-W. Kim, A wearable piezocapacitive pressure sensor with a single layer of silver nanowire-based elastomeric composite electrodes, J. Mater. Chem. A 4 (27) (2016) 10435–10443.

[3] C.S. Boland, U. Khan, G. Ryan, S. Barwich, R. Charifou, A. Harvey, C. Backes, Z. Li, M.S. Ferreira, M.E. Möbius, Sensitive electromechanical sensors using viscoelastic graphene-polymer nanocomposites, Science 354 (6317) (2016) 1257–1260.

[4] J. Zhao, G. Wang, R. Yang, X. Lu, M. Cheng, C. He, G. Xie, J. Meng, D. Shi, G. Zhang, Tunable piezoresistivity of nanographene films for strain sensing, ACS Nano 9 (2) (2015) 1622–1629.

[5] M. Ha, S. Lim, J. Park, D.-S. Um, Y. Lee, H. Ko, Bioinspired interlocked and hierarchical design of ZnO nanowire arrays for static and dynamic pressure-sensitive electronic skins, Adv. Funct. Mater. 25 (19) (2015) 2841–2849.

[6] Y. Qin, X. Wang, Z.L. Wang, Microfibre-nanowire hybrid structure for energy scavenging, Nature 451 (7180) (2008) 809–813.

[7] H. Chang, S. Kim, S. Jin, S.-W. Lee, G.-T. Yang, K.-Y. Lee, H. Yi, Ultrasensitive and highly stable resistive pressure sensors with biomaterial-incorporated interfacial layers for wearable health-monitoring and human-machine interfaces, ACS Appl. Mater. Interfaces 10 (1) (2018) 1067–1076.

[8] M. Ha, S. Lim, H. Ko, Wearable and flexible sensors for user-interactive health-monitoring devices, J. Mater. Chem. B 6 (24) (2018) 4043–4064.

[9] Y.-Q. Li, W.-B. Zhu, X.-G. Yu, P. Huang, S.-Y. Fu, N. Hu, K. Liao, Multifunctional wearable device based on flexible and conductive carbon sponge/poly-dimethylsiloxane composite, ACS Appl. Mater. Interfaces 8 (48) (2016) 33189–33196.

[10] Y. Gao, H. Ota, E.W. Schaler, K. Chen, A. Zhao, W. Gao, H.M. Fahad, Y. Leng, A. Zheng, F. Xiong, C. Zhang, L.-C. Tai, P. Zhao, R.S. Fearing, A. Javey, Wearable microfluidic diaphragm pressure sensor for health and tactile touch monitoring, Adv. Mater. 29 (39) (2017) 1701985.

[11] Z. Lou, S. Chen, L. Wang, R. Shi, L. Li, K. Jiang, D. Chen, G. Shen, Ultrasensitive and ultraflexible e-skins with dual functionalities for wearable electronics, Nano Energy 38 (2017) 28–35.

[12] H. Mai, R. Mutlu, C. Tawk, G. Alici, V. Sencadas, Ultra-stretchable MWCNT-ecoflex piezoresistive sensors for human motion detection applications, Compos. Sci. Technol. 173 (2019) 118–124.

[13] Z. Zhan, R. Lin, V.-T. Tran, J. An, Y. Wei, H. Du, T. Tran, W. Lu, Paper/carbon nanotube-based wearable pressure sensor for physiological signal acquisition and soft robotic skin, ACS Appl. Mater. Interfaces 9 (43) (2017) 37921–37928.

[14] Z. Ji, H. Zhu, H. Liu, N. Liu, T. Chen, Z. Yang, L. Sun, The design and characterization of a flexible tactile sensing array for robot skin, Sensors 16 (12) (2016) 2001.

[15] J. Park, Y. Lee, J. Hong, M. Ha, Y.-D. Jung, H. Lim, S.Y. Kim, H. Ko, Giant tunneling piezoresistance of composite elastomers with interlocked microdome arrays for ultrasensitive and multimodal electronic skins, ACS Nano 8 (5) (2014) 4689–4697.

[16] G. Ge, Y. Cai, Q. Dong, Y. Zhang, J. Shao, W. Huang, X. Dong, A flexible pressure sensor based on rGO/polyaniline wrapped sponge with tunable sensitivity for human motion detection, Nanoscale 10 (21) (2018) 10033–10040.

[17] K.Y. Lee, J. Chun, J.H. Lee, K.N. Kim, N.R. Kang, J.Y. Kim, M.H. Kim, K.S. Shin, M.K. Gupta, J.M. Baik, S.W. Kim, Hydrophobic sponge structure-based triboelectric nanogenerator, Adv. Mater. 26 (29) (2014) 5037–5042.

[18] K.Y. Lee, M.K. Gupta, S.-W. Kim, Transparent flexible stretchable piezoelectric and triboelectric nanogenerators for powering portable electronics, Nano Energy 14 (2015) 139–160.

[19] X. Chen, X. Han, Q.D. Shen, PVDF-based ferroelectric polymers in modern flexible electronics, Adv. Electron. Mater. 3 (5) (2017) 1600460.

[20] P. Hu, L. Yan, C. Zhao, Y. Zhang, J. Niu, Double-layer structured PVDF nanocomposite film designed for flexible nanogenerator exhibiting enhanced piezoelectric output and mechanical property, Compos. Sci. Technol. 168 (2018) 327–335.

[21] T. Li, H. Luo, L. Qin, X. Wang, Z. Xiong, H. Ding, Y. Gu, Z. Liu, T. Zhang, Flexible capacitive tactile sensor based on micropatterned dielectric layer, Small 12 (36) (2016) 5042–5048.

[22] F. Ke, Y. Liu, H. Xu, Y. Ma, S. Guang, F. Zhang, N. Lin, M. Ye, Y. Lin, X. Liu, Flower-like polyaniline/graphene hybrids for high-performance supercapacitor, Compos. Sci. Technol. 142 (2017) 286–293.

[23] H. He, Y. Fu, W. Zang, Q. Wang, L. Xing, Y. Zhang, X. Xue, A flexible self-powered T-ZnO/PVDF/fabric electronic-skin with multi functions of tactile-perception, atmosphere-detection and self-clean, Nano Energy 31 (2017) 37–48.

[24] S. Xu, Y. Qin, C. Xu, Y. Wei, R. Yang, Z.L. Wang, Self-powered nanowire devices, Nat. Nanotechnol. 5 (5) (2010) 366–373.

[25] Y. Mao, P. Zhao, G. McConohy, H. Yang, Y. Tong, X. Wang, Sponge-like piezoelectric polymer films for scalable and integratable nanogenerators and self-powered electronic systems, Adv. Energy. Mater. 4 (7) (2014) 1301624.

[26] C. Yan, X. Wang, M. Cui, J. Wang, W. Kang, C.Y. Foo, P.S. Lee, Stretchable silver-zinc batteries based on embedded nanowire elastic conductors, Adv. Energy. Mater. 4 (5) (2014) 1301396.

[27] G. Kettlgruber, M. Kaltenbrunner, C.M. Siket, R. Moser, I.M. Graz, R. Schwödiauer, S. Bauer, Intrinsically stretchable and rechargeable batteries for self-powered stretchable electronics, J. Mater. Chem. A 1 (18) (2013) 5505–5508.

[28] M. Koo, K.I. Park, S.H. Lee, M. Suh, D.Y. Jeon, J.W. Choi, K. Kang, K.J. Lee, Bendable inorganic thin-film battery for fully flexible electronic systems, Nano Lett. 12 (9) (2012) 4810–4816.

[29] C. Wang, K. Xia, M. Zhang, M. Jian, Y. Zhang, An all-silk-derived dual-mode E-skin for simultaneous temperature–pressure detection, ACS Appl. Mater. Interfaces 9 (45) (2017) 39484–39492.

[30] F. Zhang, Y. Zang, D. Huang, C.-a. Di, D. Zhu, Flexible and self-powered temperature–pressure dual-parameter sensors using microstructure-frame-supported organic thermoelectric materials, Nat. Commun. 6 (2015) 8356.

[31] B.W. An, S. Heo, S. Ji, F. Bien, J.-U. Park, Transparent and flexible fingerprint sensor array with multiplexed detection of tactile pressure and skin temperature, Nat. Commun. 9 (1) (2018) 2458.

[32] M. Melzer, J.I. Mönch, D. Makarov, Y. Zabila, G.S. Cañón Bermúdez, D. Karnaushenko, S. Baunack, F. Bahr, C. Yan, M. Kaltenbrunner, Wearable magnetic field sensors for flexible electronics, Adv. Mater. 27 (7) (2015) 1274–1280.

[33] Z. Ma, Y. Miao, Y. Li, H. Zhang, B. Li, Y. Cao, J. Yao, A highly sensitive magnetic field sensor based on a tapered microfiber, IEEE Photonics J 10 (4) (2018) 1–8.

[34] A. Tekgül, M. Alper, H. Kockar, Simple electrodepositing of CoFe/Cu multilayers: effect of ferromagnetic layer thicknesses, J. Magn. Magn. Mater. 421 (2017) 472–476.

[35] F. Chen, Y. Jiang, L. Zhang, L. Jiang, S. Wang, Fiber optic refractive index and magnetic field sensors based on microhole-induced inline Mach–Zehnder interferometers, Meas. Sci. Technol. 29 (4) (2018) 045103.

[36] P. Huang, Y.-Q. Li, X.-G. Yu, W.-B. Zhu, S.-Y. Nie, H. Zhang, J.-R. Liu, N. Hu, S.-Y. Fu, Bioinspired flexible and highly responsive dual-mode strain/magnetism composite sensor, ACS Appl. Mater. Interfaces 10 (13) (2018) 11197–11203.

[37] Y.-F. Liu, Y.-F. Fu, Y.-Q. Li, P. Huang, C.-H. Xu, N. Hu, S.-Y. Fu, Bio-inspired highly flexible dual-mode electronic cilia, J. Mater. Chem. B 6 (6) (2018) 896–902.

[38] Q. Zhang, Y. Du, Y. Sun, K. Zhuo, J. Ji, Z. Yuan, W. Zhang, S. Sang, A flexible magnetic field sensor based on AgNWs & MNs-PDMS, Nanoscale Res. Lett. 14 (1) (2019) 27.

[39] Y. Xu, X. Gong, S. Xuan, W. Zhang, Y. Fan, A high-performance magnetorheological material: preparation, characterization and magnetic-mechanic coupling properties, Soft Matter 7 (11) (2011) 5246–5254.

[40] J. Xu, S. Xuan, H. Pang, X. Gong, The strengthening effect of 1D carbon materials on magnetorheological plastomers: mechanical properties and conductivity, Smart Mater. Struct. 26 (3) (2017) 035044.

[41] Y. Xu, X. Gong, T. Liu, S. Xuan, Magneto-induced microstructure characterization of magnetorheological plastomers using impedance spectroscopy, Soft Matter 9 (32) (2013) 7701–7709.

[42] Y. Xu, X. Gong, S. Xuan, Soft magnetorheological polymer gels with controllable rheological properties, Smart Mater. Struct. 22 (7) (2013) 075029.

[43] H. Pang, S. Xuan, T. Liu, X. Gong, Magnetic field dependent electro-conductivity of the graphite doped magnetorheological plastomers, Soft Matter 11 (34) (2015) 6893–6902.

[44] M.K. Shabdin, A. Rahman, M. Azizi, S.A. Mazlan, N.M. Hapipi, D. Adiputra, A. Aziz, S. Aishah, I. Bahiuddin, S.-B. Choi, Material characterizations of Gr-based magnetorheological elastomer for possible sensor applications: rheological and resistivity properties, Materials 12 (3) (2019) 391.

[45] T. Tian, W. Li, G. Alici, H. Du, Y. Deng, Microstructure and magnetorheology of graphite-based MR elastomers, Rheol. Acta 50 (9–10) (2011) 825–836.

[46] W. Li, Z. Liang, Z. Lu, X. Tao, K. Liu, H. Yao, Y. Cui, Magnetic field-controlled lithium polysulfide semiliquid battery with ferrofluidic properties, Nano Lett. 15 (11) (2015) 7394–7399.

[47] E.E. Keaveny, M.R. Maxey, Modeling the magnetic interactions between paramagnetic beads in magnetorheological fluids, J. Comput. Phys. 227 (22) (2008) 9554–9571.

[48] T. Liu, X. Gong, Y. Xu, S. Xuan, W. Jiang, Simulation of magneto-induced rearrangeable microstructures of magnetorheological plastomers, Soft Matter 9 (42) (2013) 10069–10080.

[49] V.A. Parsegian, Van der Waals forces: a handbook for biologists, chemists, engineers, and physicists, Cambridge University Press, 2005.

[50] D. Klingenberg, C. Olk, M. Golden, J. Ulicny, Effects of nonmagnetic interparticle forces on magnetorheological fluids, J. Phys. Condens. Matter 22 (32) (2010) 324101.

[51] A. Beris, J. Tsamopoulos, R. Armstrong, R. Brown, Creeping motion of a sphere through a Bingham plastic, J. Fluid Mech. 158 (1985) 219–244.

[52] J. Blackery, E. Mitsoulis, Creeping motion of a sphere in tubes filled with a Bingham plastic material, J. Non-Newtonian Fluid Mech. 70 (1–2) (1997) 59–77.